JCTC Journal of Chemical Theory and Computation

pubs.acs.org/JCTC Article

Nonlocal Functionals Inspired by the Strongly Interacting Limit of DFT: Exact Constraints and Implementation

Stefan Vuckovic* and Hilke Bahmann*

Cite This: J. Chem. Theory Comput. 2023, 19, 6172−6184 Read Online

ACCESS | Metrics & More | Article Recommendations | Supporting Information

ABSTRACT: Capturing strong correlation effects remains a key challenge for the development of improved exchange−correlation (XC) functionals in density functional theory. The recently proposed multiple radii functional (MRF) [*J. Phys. Chem. Lett.* **2017**, *8*, 2799; *J. Chem. Theory Comput.* **2019**, *15*, 3580] was designed to capture strong correlation effects seamlessly, as its mathematical structure draws from that of the exact XC functional in the limit of infinite correlations. The MRF functional provides a framework for building approximations along the density-fixed adiabatic connection, delivers accurate XC energy densities in the standard DFT gauge (same as that of the exact exchange energy density), and is free of one-electron self-interaction errors. To facilitate the development of XC functionals based on the MRF, we examine the behavior of the MRF functional when applied to uniform and scaled densities and consider how it can be made exact for the uniform electron gas. These theoretical insights are then used to build improved forms for the *fluctuation function*, an object that defines XC energy densities within the MRF framework. We also show how the MRF fluctuation function for physical correlation can be easily readjusted to accurately capture the XC functional in the limit of infinite correlations, demonstrating the versatility of MRF for building approximations for different correlation regimes. We describe the implementation of MRF using densities expanded on Gaussian basis sets, which improves the efficiency of previous grid-based MRF implementations.

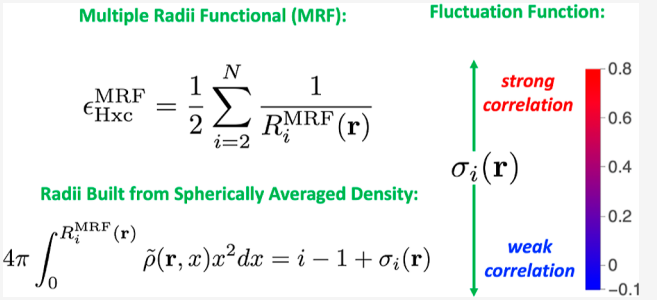

1. INTRODUCTION

A vast majority of electronic structure calculations across disciplines ranging from biology to materials science are done by density functional theory (DFT).[1−4] Within the Kohn−Sham DFT (KS DFT), the only, but crucial, piece that has to be approximated is the exchange−correlation (XC) functional. Despite the tremendous successes of DFT, the description of strong correlation electronic effects remains the major challenge in the development of new XC approximations.[5−9] One can argue that the insufficient accuracy and not uncommon qualitative failures of the standard DFT for strong correlations[1,6,7] can be traced back to the limited number of building blocks that standard DFT uses for XC approximations.[8,9] These building blocks (or features) form the so-called "Jacob's ladder" as formulated by Perdew.[10,11] The complexity and cost of the features increase as we climb up Jacob's ladder, where at the bottom rung we find the density; then the density gradient and its Laplacian (or kinetic energy density) in the middle rungs; and the KS occupied and unoccupied orbitals in the top rungs.[10,11]

Nearly all currently available XC approximations are built from these Jacob's ladder features, including the very recent XC models obtained from machine learning (ML).[8,12] This includes recent DM21 functional designed to reduce the errors of approximate XC functionals for fractional spins and fractional charges.[13] Even though the DM21 development has made a breakthrough in using ML to optimize XC approximations, DM21 still suffers from deficiencies inherent to the limitations of the Jacob's ladder features it uses. For example, upon dissociation of H_2, DM21 gets the region around equilibrium right (weak correlation) as well as the dissociation limit (strong correlation) as it has been trained on its dissociation limit.[13] However, describing homonuclear diatomics at intermediate bond distances (e.g., about 3 Å for H_2) can be even more challenging than the dissociation limit due to the delicate interplay between weak (dynamical) and strong (static) correlation.[14] For the intermediate distances, DM21 displays a large unphysical bump in the H_2 dissociation curve.[13] This deficiency of DM21 can be fixed by symmetry breaking or fractional KS occupations, but the two approaches would also fix, e.g., B3LYP's H_2 dissociation curves.[15,16] The challenge is thus to build an XC approximation capturing strong correlation in the standard KS framework without artificial symmetry breaking.

Received: April 21, 2023
Published: August 23, 2023

https://doi.org/10.1021/acs.jctc.3c00437
J. Chem. Theory Comput. 2023, 19, 6172−6184

A way forward in ML of XC approximations able to capture different correlation regimes (from weak to strong) is to use fully nonlocal features (i.e., containing information about the electronic density everywhere).[8,9] Then the question arises: what is the form of the fully nonlocal features that can be used? While some very recent ML XC models attempted to make use of different nonlocal features,[17−21] the strongly interacting limit (SIL) of DFT provides a natural and theoretically firm ground for the development and utilization of the fully nonlocal features.[9] Specifically, the rigorous mathematical treatment of the SIL reveals that the building blocks of the exact XC functionals arising from the SIL are very different from the standard Jacob's ladder features.[9,22−26] Instead of semilocal quantities and KS orbitals that form the Jacob's ladder, in the SIL, we see specific integrals of the density encoding fully nonlocal information. For general (3D) geometries, computing the exact SIL is prohibitively costly,[9] which in turn inspired the construction of functionals (with the N^3 scaling) that either approximate the SIL or are inspired by the SIL features.[9] For example, the nonlocal radius[27] and shell model[28] have been proposed to approximate the SIL and retain some of its nonlocality. On the other hand, the recently proposed fully nonlocal multiple radii functional (MRF)[29−31] draws from the main structural motifs of the SIL but approximates electronic energy at the physical regime instead of the strongly interacting one.

The main building block for MRF is the following integral

$$N_e([\rho];\, \mathbf{r},\, u) = 4\pi \int_0^u \tilde{\rho}(\mathbf{r},\, x) x^2 \, \mathrm{d}x \tag{1}$$

over the spherically averaged density

$$\tilde{\rho}(\mathbf{r},\, u) = \frac{1}{4\pi} \int \rho(\mathbf{r} + \mathbf{u}) \, \mathrm{d}\mathbf{\Omega}_\mathbf{u} \tag{2}$$

where $\rho(\mathbf{r})$ is the usual (one-electron) density. Alternatively, we can write $N_e([\rho];\, \mathbf{r},\, u)$ directly in terms of ρ via the Heaviside Θ function: $N_e(u;\, \mathbf{r}) = \int \Theta(|\mathbf{r} - \mathbf{r}'| - u)\rho(\mathbf{r}') \, \mathrm{d}\mathbf{r}'$, where $\Theta(x) = \{1\ \forall\ x \geq 0,\ 0\ \forall\ x < 0\}$ is the Heaviside step function. By encoding fully nonlocal information through $N_e([\rho];\, \mathbf{r},\, u)$, MRF has a range of advantages missed by standard functional. It is free of one-electron self-interaction error, captures electronic correlation arising upon bonds stretching in a seamless manner, and provides correlation energy densities within the standard DFT definition (i.e., *gauge*) that are fully compatible with the exact exchange energy densities.[29−31] These good features of MRF arise already by its construction and thus provide a different starting point for building a new class of XC functional approximations that overcome the drawbacks of current ones. This makes the use of MRF features highly appealing for ML of XC approximations (or alternatively using ML to improve MRF). However, certain challenges have to be addressed before we can get to that stage. First, due to its radically different mathematical structure, one cannot follow standard routes used for improving semilocal functionals to refine MRF. For example, incorporation of the exact constraints is a standard "Perdew-school" route for refining XC functional approximations.[5,32] Making a semilocal approximation exact for the uniform electron gas (UEG) is trivial for semilocal approximations,[32,33] but a different mathematical structure of MRF makes the imposition of this and other constraints more involved (see e.g., refs 34−37 for in-depth discussions on the relevance of the UEG constraint for both solids and molecules). Second, despite its affordable scaling (N^3), the full nonlocality of MRF and its underlying features require more implementation effort to make them readily available in quantum-chemical codes.

In the present paper, we overcome these two crucial challenges for the use of MRF features or MRF itself for the development of (ML) fully nonlocal functionals and making DFT accurate for strongly correlated systems. First, we consider how well the existing MRF forms satisfy certain exact constraints (e.g., when applied to scaled and uniform densities), and how these constraints can be incorporated intothem. Then we use these insights to improve MRF by refining and analyzing the so-called *fluctuation function*, an object that defines the XC functional within MRF. Then we focus on the practical aspects, develop the improved MRF integral package, and implement MRF into a development version of the TURBOMOLE program.[38] The key idea is to obtain a flexible implementation that will easily accommodate improvements through refined forms for the fluctuation function. The main computational bottleneck for MRF is the calculation of the density integral of eq 1. We overcome this issue by using the analytical integrals pertaining to eq 1 over the standard Gaussian basis functions. In addition to the MRF itself, we also implement the MRF *reverse machinery*,[30] which we use to make the exchange part of the MRF deliver exact exchange energy densities, and then we use this as the starting point for building the MRF correlation functional.

The paper is organized as follows: The relevant theoretical background is given in Section 2. The behavior of MRF for uniformly scaled densities and the UEG are then studied in Sections 3 and 4, respectively. These insights are then used in Section 5 to analyze how MRF can be improved. The details for the implementation of MRF are given in Section 6, and discussion and numerical examples are given in Section 7, while Section 8 is devoted to conclusions and outlooks. Hartree atomic units are used throughout this paper unless otherwise specified.

2. BACKGROUND

2.1. Exact Exchange−Correlation Functional. For a given $\rho(\mathbf{r})$, an exact density-fixed adiabatic connection (AC) expression for the XC energy is given by[39−41]

$$E_{XC}[\rho] = \int_0^1 W_\lambda[\rho] \, \mathrm{d}\lambda \tag{3}$$

where $W_\lambda[\rho]$ is the global AC integrand that we can write in terms of the local quantities as[29,41−43]

$$W_\lambda[\rho] = \int w_\lambda(\mathbf{r})\rho(\mathbf{r}) \, \mathrm{d}\mathbf{r} \tag{4}$$

where $w_\lambda(\mathbf{r})$ is the XC energy density arising from the $\Psi_\lambda[\rho]$ fermionic wavefunction that integrates to $\rho(\mathbf{r})$ and minimizes the sum of the kinetic energy $\hat{T}$ and the electron−electron repulsion $\hat{V}_{ee}$ scaled by the non-negative coupling constant λ. To link $w_\lambda(\mathbf{r})$ with $\Psi_\lambda[\rho]$, we define first the spherically averaged pair density, $P_2^\lambda(\mathbf{r},\, u)$, which is obtained from $\Psi_\lambda[\rho]$ through

$$P_2^\lambda(\mathbf{r},\, u) = \frac{N(N-1)}{4\pi} \times \sum_{\sigma_1 \ldots \sigma_N} \int |\Psi_\lambda(\mathbf{r}\sigma_1,\, (\mathbf{r} + \mathbf{u})\sigma_2,\, \mathbf{r}_3\sigma_3, \ldots,\, \mathbf{r}_N\sigma_N)|^2 \, \mathrm{d}\mathbf{\Omega}_\mathbf{u} \, \mathrm{d}\mathbf{r}_3 \ldots \mathrm{d}\mathbf{r}_N \tag{5}$$

In terms of $P_2^\lambda(\mathbf{r},\, u)$, we define the spherically averaged XC hole

https://doi.org/10.1021/acs.jctc.3c00437
J. Chem. Theory Comput. 2023, 19, 6172−6184

$$h_{xc}^{\lambda}(\mathbf{r}, u) = \frac{P_2^{\lambda}(\mathbf{r}, u)}{\rho(\mathbf{r})} - \tilde{\rho}(\mathbf{r}, u) \tag{6}$$

Finally, $w_\lambda(\mathbf{r})$ reads as[42,44,45]

$$w_\lambda(\mathbf{r}) = \frac{1}{2}\int_0^\infty \frac{h_{xc}^{\lambda}(\mathbf{r}, u)}{u} 4\pi u^2 \, du \tag{7}$$

An important note is that the XC energy density is not uniquely defined,[29,41−43] but we stick here to its definition given by eq 7, that of the electrostatic potential of the XC hole.

2.2. Multiple-Radii Functional (MRF). In this section, the cornerstones of the MRF model are briefly summarized to provide a basic understanding of the challenges in its implementation and its further improvement. MRF approximates $w_\lambda(\mathbf{r})$ as[29−31]

$$w_\lambda^{\mathrm{MRF}}(\mathbf{r}) = \frac{1}{2}\sum_{i=2}^{N} \frac{1}{R_i^{\lambda}([\rho]; \mathbf{r})} - \frac{1}{2} v_H(\mathbf{r}) \tag{8}$$

where $R_i^{\lambda}([\rho]; \mathbf{r})$ are the *radii* or effective distances between a reference electron at $\mathbf{r}$ and the remaining $N - 1$ electrons. $R_i^{\lambda}([\rho]; \mathbf{r})$ are defined in terms of the inverse of the electron number function of eq 1

$$R_i^{\lambda}([\rho]; \mathbf{r}) = N_e^{-1}(\mathbf{r}, i - 1 + \sigma_i^{\lambda}(\mathbf{r})) \tag{9}$$

where σ_i^{λ} is the *fluctuation function*. Combining eqs 4, 8, and 9, we obtain

$$W_\lambda^{\mathrm{MRF}}[\rho] = \frac{1}{2}\int d\mathbf{r}\rho(\mathbf{r})\sum_{i=2}^{N} \frac{1}{N_e^{-1}(\mathbf{r}, i - 1 + \sigma_i^{\lambda}(\mathbf{r}))} - U[\rho] \tag{10}$$

where $U[\rho] = 1/2\int\rho(\mathbf{r})v_H(\mathbf{r})\, d\mathbf{r}$ is the Hartree energy. By eq 10, MRF reduces approximating $E_{xc}[\rho]$ by finding σ_i^{λ}. The underlying idea is that it is much easier to approximate $\sigma^{\lambda}(\mathbf{r})$ than the corresponding energy densities, as the former is bounded in between −1 and 1, changes little locally in a given system and across systems,[29−31] and can be represented through very simple mathematical forms. For example, setting $\sigma_i^{\lambda=1} = 0$ already gives accurate atomic energy densities at the full coupling strength. In refs 29−31, the following form for $\sigma_i^{\lambda=1}$ has been considered

$$\sigma_i^{\lambda=1}(\mathbf{r}) = \frac{1}{2} e^{-bS_i(\mathbf{r})^2} \tag{11}$$

where $b = 5$ has been chosen to optimize electronic repulsion energy for He, and where $S_i(\mathbf{r})$

$$S_i(\mathbf{r}) = \left.\frac{\partial N_e(\mathbf{r}, x)}{\partial x}\right|_{x=N_e^{-1}(\mathbf{r},i-1)} = 4\pi a_i(\mathbf{r})^2\tilde{\rho}(\mathbf{r}, a_i(\mathbf{r})) \tag{12}$$

gives the information on the radial spherically averaged density of the i-th neighboring electron at their *initial* distances (radii) from the reference electron

$$a_i(\mathbf{r}) = N_e^{-1}(\mathbf{r}, i - 1) \tag{13}$$

In this way, $\sigma_i^{\lambda}(\mathbf{r})$ can push away or bring the i-th electron closer to the reference electron from these initial a_i distances.

The σ of eq 12 already gives accurate atomic energy densities and captures the physics of bond breaking. Furthermore, even though it is built for 3D systems, the same form gives comparable accuracy for reduced dimensionalities.[31] The MRF's $P_{2,\lambda}([\rho]; \mathbf{r}, u)$ that gives rise to eq 8 is given by

$$P_{2,\lambda}^{\mathrm{MRF}}([\rho]; \mathbf{r}, u) = \frac{1}{4\pi u^2}\sum_{i=2}^{N} \rho(\mathbf{r})\delta(u - R_i^{\lambda}(\mathbf{r})) \tag{14}$$

where δ is the Dirac delta function. As $P_{2,\lambda}^{\mathrm{MRF}}([\rho]; \mathbf{r}, u)$ is given by the sum of δ functions, it is not meant to approximate the exact $P_{2,\lambda}([\rho]; \mathbf{r}, u)$ at finite λ values. Instead, it *only* serves as the auxiliary object that delivers $w_\lambda^{\mathrm{MRF}}(\mathbf{r})$, since this is the object that MRF aims to accurately approximate. In other words, $P_{2,\lambda}^{\mathrm{MRF}}([\rho]; \mathbf{r}, u)$ is not an approximation of the exact $P_{2,\lambda}([\rho]; \mathbf{r}, u)$ at finite λ, but the electrostatic potential of the former is an approximation to that of the latter.

2.3. Reverse MRF Machinery. In special cases, ($N = 2$ any λ and $\lambda \to \infty$ for any N), there is a one-to-one correspondence between $\sigma_i^{\lambda}(\mathbf{r})$ and $w_\lambda(\mathbf{r})$. For these special cases, one can use the exact $w_\lambda(\mathbf{r})$ (available for small systems), translate it to "exact" $\sigma_i^{\lambda}(\mathbf{r})$, and then use those to guide the improvement of MRF. In general, there is no one-to-one correspondence between $\sigma_i^{\lambda}(\mathbf{r})$ and $w_\lambda(\mathbf{r})$. This is circumvented within the so-called the *reversed MRF machinery* (rm-MRF),[30] where one approximates $\sigma_i^{\lambda}(\mathbf{r})$ by $\tilde{\sigma}^{\lambda}(\mathbf{r})$, which is the constant, i-averaged fluctuation function. With this approximation, we get a one-to-one correspondence between $\tilde{\sigma}^{\lambda}(\mathbf{r})$ and $w_\lambda(\mathbf{r})$

$$\sum_{i=2}^{N} N_e^{-1}(\mathbf{r}, i - 1 + \tilde{\sigma}^{\lambda}(\mathbf{r})) = \frac{1}{v_H(\mathbf{r}) + 2w_\lambda(\mathbf{r})} \tag{15}$$

Equation 15 enables us to reverse engineer $\tilde{\sigma}^{\lambda}(\mathbf{r})$ by using $w_\lambda(\mathbf{r})$ input energy density, and this is what specifically we refer here to rm-MRF. This already enables us to take the exact exchange energy density $w_{\lambda=0}(\mathbf{r})$, translate it to $\tilde{\sigma}^{\lambda=0}(\mathbf{r})$, and then use the latter as the starting point for building the correlation part of the MRF functional on the top of the exact exchange. In Section 6, we also give details for the implementation of rm-MRF.

3. MRF SCALING RELATIONS

Consider the usual uniform coordinate scaling of the density[46,47]

$$\rho_\gamma(\mathbf{r}) = \gamma^3\rho(\gamma\mathbf{r}) \tag{16}$$

where γ is a non-negative number. A range of DFT quantities scale linearly with γ

$$X[\rho_\gamma] = \gamma X[\rho] \tag{17}$$

This holds for the Hartree energy $U[\rho_\gamma]$, $W_\lambda[\rho_\gamma]$ integrand of eq 3 in the $\lambda \to 0$ (exact exchange) and $\lambda \to \infty$ limit.[46,47] The scaling of $W_\lambda[\rho_\gamma]$ in between the two limits is non-trivial, and it is known that $E_{XC}[\rho]$ and $W_{\lambda=1}[\rho]$ do not scale linearly with γ in general.[46]

To examine the behavior of MRF under uniform density scaling, we first check the scaling of its ingredients. By eqs 2 and 16, the spherically averaged density scales as

$$\tilde{\rho}_\gamma(\mathbf{r}, u) = \gamma^3\tilde{\rho}(\gamma\mathbf{r}, \gamma u) \tag{18}$$

Thus, N_e of eq 1 obeys

$$N_e([\rho_\gamma]; \mathbf{r}, u) = N_e([\rho]; \gamma\mathbf{r}, \gamma u) \tag{19}$$

In what follows, we show that if the fluctuation function obeys

$$\sigma_i^{\lambda}([\rho_\gamma]; \mathbf{r}) = \sigma_i^{\lambda}([\rho]; \gamma\mathbf{r}) \tag{20}$$

https://doi.org/10.1021/acs.jctc.3c00437
J. Chem. Theory Comput. 2023, 19, 6172−6184

the resulting $W_\lambda^{\mathrm{MRF}}[\rho_\gamma]$ must scale linearly with γ (i.e., satisfies eq 17). To deduce the scaling of the radii resulting from the fluctuation functions obeying eq 20, we use the implicit definition of the radii following from eq 9

$$N_e([\rho];\, \mathbf{r},\, R_i^\lambda(\mathbf{r})) = i - 1 + \sigma_i^\lambda(\mathbf{r}) \tag{21}$$

Combining eqs 20 and 21, we obtain

$$N_e([\rho_\gamma];\, \mathbf{r},\, R_i^\lambda([\rho_\gamma];\, \mathbf{r})) = N_e([\rho];\, \gamma\mathbf{r},\, R_i^\lambda([\rho];\, \gamma\mathbf{r})) \tag{22}$$

Inserting now eq 19 into the l.h.s. of eq 22, we obtain

$$N_e([\rho];\, \gamma\mathbf{r},\, \gamma R_i^\lambda([\rho_\gamma];\, \mathbf{r})) = N_e([\rho];\, \gamma\mathbf{r},\, R_i^\lambda([\rho];\, \gamma\mathbf{r})) \tag{23}$$

which, in turn, dictates the following scaling of the radii

$$R_i^\lambda([\rho_\gamma];\, \mathbf{r}) = \frac{1}{\gamma} R_i^\lambda([\rho];\, \gamma\mathbf{r}) \tag{24}$$

These radii, arising from the fluctuation function satisfying the scaling relation of eq 20, dictate the following scaling of $W_\lambda^{\mathrm{MRF}}[\rho]$ of eq 10

$$\begin{aligned} W_\lambda^{\mathrm{MRF}}[\rho_\gamma] &= \frac{1}{2}\int \mathrm{d}\mathbf{r}\rho_\gamma(\mathbf{r})\sum_{i=2}^{N}\frac{1}{R_i^\lambda([\rho_\gamma];\, \mathbf{r})} - U[\rho_\gamma] \\ &= \frac{1}{2}\int \mathrm{d}\mathbf{r}\gamma^3\rho(\gamma\mathbf{r})\sum_{i=2}^{N}\frac{\gamma}{R_i^\lambda([\rho];\, \gamma\mathbf{r})} - \gamma U[\rho] \end{aligned} \tag{25}$$

which reduces to

$$W_\lambda^{\mathrm{MRF}}[\rho_\gamma] = \gamma W_\lambda^{\mathrm{MRF}}[\rho] \tag{26}$$

As said, it is known that the exact $W_{\lambda=1}[\rho]$ does not, in general, obey eq 17. The same is true for the scaling of $W_{\lambda=1}^{\mathrm{MRF}}[\rho]$ within the original fluctuation function for $\lambda = 1$ (eq 11).

4. MRF FOR THE UNIFORM ELECTRON GAS

In ref 29, the very basic properties of the MRF functional for the UEG as a paradigm for extended systems have been studied. In this section, we give a full derivation of the MRF functional for the UEG, numerically examine the properties of the MRF for the UEG, and consider how the functional can be made exact for the UEG.

For the UEG with the density $\rho = \left(\frac{4}{3}\pi r_s^3\right)^{-1}$, eq 8 becomes

$$w_\lambda^{\mathrm{MRF}}(r_s) = \frac{1}{2}\sum_{i=2}^{N}\frac{1}{R_i^\lambda([\rho])} - \frac{1}{2}\int_0^\infty 4\pi u\rho\, \mathrm{d}u \tag{27}$$

To take the thermodynamic limit, we consider a sphere of volume $\Omega = \frac{4}{3}\pi L^3$ containing N electrons. Since $\rho = N/\Omega$, the radius of the sphere will be $L = r_s N^{1/3}$. Expressing ρ and L in terms of r_s and N, the second term on the r.h.s. of eq 27 becomes $\frac{3}{2r_s^3}\int_0^L u\, \mathrm{d}u = \frac{3}{4r_s^3}L^2$. Since $L = r_s N^{1/3}$, eq 27 becomes

$$w_\lambda^{\mathrm{MRF}}(r_s) = \lim_{N\to\infty}\left[\frac{1}{2}\left(\sum_{i=2}^{N}\frac{1}{R_i^\lambda([\rho])} - \frac{3}{2r_s}N^{2/3}\right)\right] \tag{28}$$

For the UEG, $N_e(\mathbf{r}, u)$ is just: $N_e(u) = u^3/r_s^3$, and its inverse is $N_e^{-1}(i-1) = r_s(i-1)^{1/3}$. Taking this into account and inserting eq 9 into eq 28, we finally obtain

$$w_\lambda^{\mathrm{MRF}}(r_s) = \lim_{N\to\infty}\left[\frac{1}{2r_s}\left(\sum_{i=2}^{N}\frac{1}{(i - 1 + \sigma_i^\lambda(r_s))^{1/3}} - \frac{3}{2}N^{2/3}\right)\right] \tag{29}$$

Splitting the summation in eq 29 into two terms, one from $i = 2$ to some $i_{\max}$ and the other from $i_{\max} + 1$ to N, we can write

$$\begin{aligned} w_\lambda(r_s)^{\mathrm{MRF}} = \frac{1}{2r_s}\Bigg(&\sum_{i=2}^{i_{\max}}\frac{1}{(i - 1 + \sigma_i^\lambda(r_s))^{1/3}} \\ &+ \lim_{N\to\infty}\Bigg[\Bigg(\sum_{i=i_{\max}+1}^{N}\frac{1}{(i - 1 + \sigma_i^\lambda(r_s))^{1/3}} \\ &- \frac{3}{2}N^{2/3}\Bigg)\Bigg]\Bigg) \end{aligned} \tag{30}$$

To evaluate eq 30 for the UEG with the fluctuation function of eq 11, we need $S_i(r_s)$, which for the UEG takes the very simple form

$$S_i = 3\frac{(i-1)^{2/3}}{r_s} \tag{31}$$

For sufficiently large $i_{\max}$ and for $\sigma_i^\lambda(r_s)$ vanishing at large N (e.g., eq 11), we can write eq 30 as

$$\begin{aligned} w_\lambda(r_s) = \frac{1}{2r_s}\Bigg(&\sum_{i=2}^{i_{\max}}\frac{1}{(i - 1 + \sigma_i^\lambda(r_s))^{1/3}} \\ &+ \lim_{N\to\infty}\left[\left(\sum_{i=i_{\max}+1}^{N}\frac{1}{(i-1)^{1/3}} - \frac{3}{2}N^{2/3}\right)\right]\Bigg) \end{aligned} \tag{32}$$

which can be re-written by using a closed form for the second term

$$w_\lambda(r_s) = \frac{1}{2r_s}\left(\sum_{i=2}^{i_{\max}}\frac{1}{(i - 1 + \sigma_i^\lambda(r_s))^{1/3}} + H\left(\frac{1}{3},\, i_{\max}\right)\right) \tag{33}$$

where $H(x, y)$ is the *analytical continuation of the Hurwitz Zeta function*,[48] which is conveniently implemented in, e.g., Wolfram Mathematica,[49] where it can be easily accessed through `HurwitzZeta[x, y]`.

In practice, small $i_{\max}$ values are needed to achieve convergence. The second term in eq 33 is a resummation, whereas the first term requires an explicit summation and is thus more expensive. Physically, this can be seen as if the reference electron interacts only with a set of $i_{\max} - 1$ neighbors, and the remaining ones are only implicitly treated. We can check the convergence of MRF for the UEG w.r.t. $i_{\max}$ by using the fluctuation function of eq 11 for $\lambda = 1$. The convergence of $w_{\lambda=1}^{\mathrm{MRF}}(r_s)$ w.r.t. $i_{\max}$ at zero spin polarization is shown in the left panel of Figure 1. We can see that for small r_s only few electrons are needed to reach the convergence (for $r_s = 10$, $i_{\max} = 5$ is more than enough, and for $r_s = 25$, $i_{\max} = 10$ is more than enough). But, for $r_s = 100$, the convergence is achieved at $i_{\max} \sim 100$. Mathematically, this is because at small r_s values $i_{\max}$ quickly becomes much larger than $\sigma_{i\geq 2}$, since when $r_s \to 0$, σ_i tends to 0 [eqs 11 and 31]. Physically, this is also an appealing feature of

https://doi.org/10.1021/acs.jctc.3c00437
J. Chem. Theory Comput. 2023, 19, 6172−6184

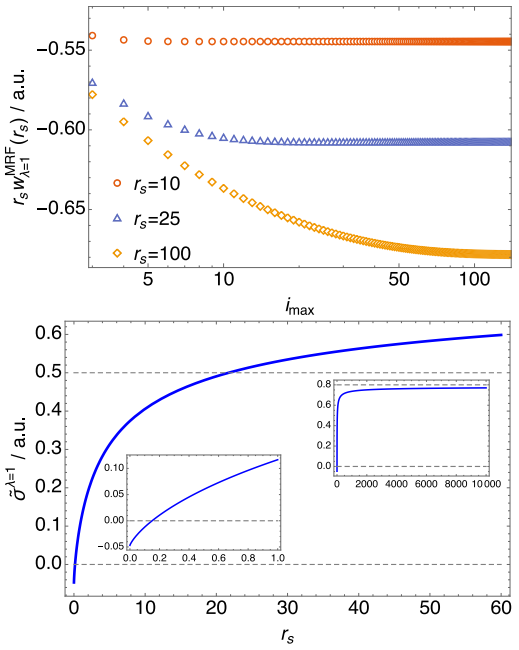

Figure 1. MRF for the UEG. Top panel: convergence of $w^{MRF}_{\lambda=1}(\mathbf{r})$ for the unpolarized UEG obtained from eq 33 w.r.t. i_{max} obtained from the fluctuation function for $\lambda = 1$ of eq 11. Bottom panel: i-averaged $\tilde{\sigma}^{\lambda=1}(r_s)$ obtained from eq 34 and exact $w_{\lambda=1}(r_s)$ [eq 16; PW92 parametrization] at different r_s values. The insets zoom in on the plots at small and large r_s values.

MRF, as larger i_{max} values are needed to achieve the convergence as correlation becomes stronger with the increase of r_s. In other words, a reference electron needs to "communicate" with more and more neighbors to describe the physics of the UEG as long-range fluctuations become more and more important as $r_s \to \infty$.

If a constant (i.e., i-averaged) $\sigma_i^{\lambda}(r_s) = \tilde{\sigma}^{\lambda}(r_s)$ is used (as in rm-MRF presented in Section 2.3), then eq 29 takes the following very simple form

$$w_{\lambda}^{MRF}(r_s) = \frac{1}{2r_s} H\left(\frac{1}{3}, 1 + \tilde{\sigma}^{\lambda}\right) \tag{34}$$

Equation 34 gives us a possibility to take the exact $w_{\lambda}(r_s)$ and reverse engineer $\tilde{\sigma}(r_s)$. At $\lambda = 0$ and zero polarization, $w_{\lambda=0}(r_s) = \epsilon_X(r_s) \approx -0.458/r_s$, yielding through eq 34

$$\tilde{\sigma}^{x}(r_s) \sim -0.0469179 \tag{35}$$

for all r_s values. We can also take the exact $w_{\lambda=1}(r_s)$ and then observe how the resulting $\tilde{\sigma}^{\lambda}(r_s)$ varies with r_s. The exact $w^{UEG}_{\lambda=1}(r_s)$ is obtained for the UEG from ϵ_{xc} through the following scaling relation

$$w_{\lambda=1}(r_s) = \frac{1}{r_s}\frac{\partial}{\partial r_s}(r_s^2 \epsilon_{xc}(r_s)) \tag{36}$$

and throughout this work we use the PW92 parametrization[50] for ϵ_{xc} and assume zero polarization.

In the right panel of Figure 1, we show the resulting $\tilde{\sigma}^{\lambda=1}$. We can see that as $r_s \to 0$, $\tilde{\sigma}^{\lambda=1} \to \tilde{\sigma}^{x}$, since $w_{\lambda=1}$ reduces to ϵ_x. As r_s increases, the correlation between electrons becomes stronger and $\tilde{\sigma}^{\lambda=1}$ increases. The range of σ values for the UEG is in line with the previous "exact" $\tilde{\sigma}^{\lambda=1}$ plots for atoms and H_2, where negative σ was observed for the exchange regimes and was around 0 for weak correlations.[29−31] When correlation becomes very strong, $\tilde{\sigma}^{\lambda=1}$ approaches 1/2 (e.g., stretched H_2). For the UEG, when $r_s \geq 19.3$, $w_{\lambda\to\infty}(\mathbf{r})$ even exceeds 1/2 and slowly tends to ∼0.8 as $r_s \to \infty$.

5. IMPROVED FLUCTUATION FUNCTIONS

5.1. Form of the New Fluctuation Function. In the present work, we consider the following fluctuation function

$$\sigma_i^{\lambda}(\mathbf{r}) = \tilde{\sigma}^{x}(\mathbf{r}) + \underbrace{\tilde{\sigma}_L^{c,\lambda}(\mathbf{r}) + \sigma_{i,NL}^{c,\lambda}(\mathbf{r})}_{\sigma_i^{c,\lambda}(\mathbf{r})} \tag{37}$$

where the first term is the exchange component and is constant (i.e., i-independent), and the last two terms are the correlation parts of the fluctuation function, where the L (*local*) term is a constant w.r.t. i, while the NL (*nonlocal*) term depends on i. The exchange $\tilde{\sigma}^{x}(\mathbf{r})$ term ensures that the MRF energy density resulting from the fluctuation function of eq 37 reduces to the exact exchange energy density when the correlation terms are omitted. The L correlation term, $\tilde{\sigma}_L^{c,\lambda}(\mathbf{r})$ we will use to impose additional exact constraints to the MRF functional (e.g., making it deliver essentially exact energetics for the UEG). The idea is to construct this term by using the standard (semi)local DFT quantities (density, its gradient, etc.).

Note here that the MRF functional is by construction fully nonlocal (eq 10), and thus its full nonlocality is still preserved even if the L term is the only one used in the fluctuation function of eq 37. Moreover, the L term in the fluctuation function also does not change the *gauge* of the underlying MRF XC energy densities, as eq 8 arising from the pair density of eq 14 ensures that the gauge of MRF XC energy densities is always that of eq 7. The NL term in the correlation part of the fluctuation function is the one that was already contained in the original MRF fluctuation function for $\lambda = 1$ (eq 11) and enables us to add extra nonlocal information through S_i, which is given by eq 11 and can be seen as "the density at the position of i-th neighbor multiplied by the spherical volume element". Thereby, the NL term captures long-range correlations and is crucial to describe the bond breaking as analyzed in ref 31. As done originally, we want to keep the NL term decreasing with S_i and keep it bounded between 0 ($S_i \to 0$) and 1/2 ($S_i \to \infty$). Through S_i, the NL term of eq 37 encodes additional nonlocal information on long-range electronic correlations but contains no local information (e.g., about the density, its gradients, etc., at the position of a reference electron at $\mathbf{r}$). We want to offset this by the L of eq 37, and as we shall see later, this term will enable us to impose additional exact constraints to the MRF functional. Now we consider the basic principles for the construction of individual terms in eq 37 for the $\lambda = 1$ and unpolarized case. The same principles would apply for other λ values and other polarizations. In eq 37, the $\tilde{\sigma}^{x}(\mathbf{r})$ term is obtained through rm-MRF from the exact $w_{\lambda=0}(\mathbf{r})$, the exact exchange energy density, which is also used in local hybrids. For the $\sigma_{i,NL}^{c,\lambda=1}(\mathbf{r})$ term, we use the original form for the fluctuation function at $\lambda = 1$ (eq 11)

$$\sigma_{i,NL}^{c,\lambda=1}(\mathbf{r}) = \frac{1}{2} e^{-bS_i(\mathbf{r})^2}; \qquad b = 5 \tag{38}$$

This form has the features that we want the NL term of eq 37 to have: it decreases with S_i and it ranges from 0 to 1/2. Originally, such form has been used as the only term for the original fluctuation function at $\lambda = 1$ (eq 11). Because of this and its

https://doi.org/10.1021/acs.jctc.3c00437
J. Chem. Theory Comput. 2023, 19, 6172−6184

simplicity, it is likely that $\sigma_{i,\mathrm{NL}}^{c,\lambda=1}(\mathbf{r})$ of eq 38 is not optimal when used with the other two terms in eq 37. However, instead of fully optimizing MRF, we aim here to better understand how we can further constrain it by using eq 37 and understand how each term of the fluctuation function of eq 37 can improve different aspects of MRF.

To complete the construction, we still need the L term of eq 37, $\tilde{\sigma}_{\mathrm{L}}^{c,\lambda=1}(\mathbf{r})$. Since we want it to primarily depend on the local density, the UEG gives us a natural choice for its construction. For this term, we cannot use $\tilde{\sigma}^{\lambda=1}(r_s) - \tilde{\sigma}^{x}$ from the right panel of Figure 1 since it was computed without the NL term, which we will need to "subtract off" to make eq 37 highly accurate for the UEG. This is what we will consider in the next section.

5.2. Making the New Fluctuation Function Exact for the UEG. To make eq 37 highly accurate for the UEG, we begin with the $\tilde{\sigma}^{x}$ term of eq 37, whose role is to reduce $w_{\lambda=1}^{\mathrm{MRF}}(\mathbf{r})$ to $w_{\lambda=0}(\mathbf{r})$ when the correlation terms are omitted. We computed this object for the UEG in Section 4, and its value is given in eq 35 and it does not depend on r_s. The NL term is given by eq 38, and the L term remains the only one to be built for $w_{\lambda=1}^{\mathrm{MRF}}(r_s)$.

With the fluctuation function of eq 37, eq 30 becomes

$$w_{\lambda=1}^{\mathrm{MRF}}(r_s) = \frac{1}{2r_s}\left(\sum_{i=2}^{i_{\max}} \frac{1}{(i-1+\tilde{\sigma}^{x}+\sigma_{i,\mathrm{NL}}^{c,\lambda=1}(r_s)+\tilde{\sigma}_{\mathrm{L}}^{c,\lambda=1}(r_s))^{1/3}} + H\left(\frac{1}{3}, i_{\max}+\tilde{\sigma}^{x}+\tilde{\sigma}_{\mathrm{L}}^{c,\lambda}(r_s)\right)\right) \tag{39}$$

where $\tilde{\sigma}^{x}$ and $\sigma_{i,\mathrm{NL}}^{c,\lambda=1}(r_s)$ are given by eqs 35 and 38, respectively. In contrast to eq 33, which holds for the σ_i vanishing at large N, the i-independent part of the fluctuation function in eq 39 is absorbed by the H function since it survives the $N \to \infty$ limit. To obtain $\tilde{\sigma}_{\mathrm{L}}^{c,\lambda}(r_s)$, we equate the r.h.s. of eq 38 to the exact $w_{\lambda=1}(r_s)$ [eq 36; PW92] and numerically solve the resulting equation for $\tilde{\sigma}_{\mathrm{L}}^{c,\lambda}(r_s)$. We use $i_{\max} = 5000$, and this $i_{\max}$ value is more than sufficient for $r_s < 1000$ to ensure the convergence of the $\tilde{\sigma}_{\mathrm{L}}^{c,\lambda}$ solutions. The resulting $\tilde{\sigma}_{\mathrm{L}}^{c,\lambda}$ data are shown in Figure 2, and we fit those to

$$\tilde{\sigma}_{\mathrm{L}}^{c,\lambda=1}(r_s) = \tilde{\sigma}_{\mathrm{UEG}}^{c,\lambda=1}(r_s) = (0.0071r_s + 0.0761)r_s \ln\left(1 + \frac{1}{0.0212r_s^2 + 0.135r_s}\right) \tag{40}$$

and we also plot the fit function in the same figure.

At small r_s, where correlation vanishes, $\tilde{\sigma}_{\mathrm{L}}^{c,\lambda=1}(r_s)$ correctly becomes 0. Note again that $\tilde{\sigma}_{\mathrm{L}}^{c,\lambda=1}(r_s)$ is made to work in tandem *only* with the specific form for its NL counterpart given in eq 38. In contrast, $\tilde{\sigma}^{\lambda=1}(r_s)$ shown in the right panel of Figure 1 is meant to work on its own without the NL part. An interesting difference between the $\tilde{\sigma}^{\lambda=1}(r_s)$ (right panel of Figure 1) and $\tilde{\sigma}_{\mathrm{L}}^{c,\lambda=1}(r_s)$ (Figure 2) can be observed for large r_s values. In the former case (no NL counterpart in σ), the saturation is very slow

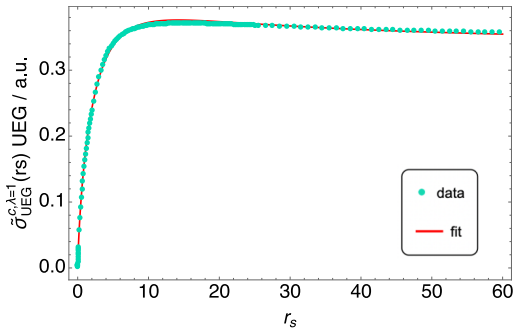

Figure 2. Datapoints with $\tilde{\sigma}_{\mathrm{L}}^{c,\lambda}$ of eq 39 delivering the PW92-parametrized $w_{\lambda=1}$ at different r_s values. The plot also shows the fit of eq 40.

at large r_s, whereas in the latter case (with NL counterpart), it is much faster and already for r_s values larger than ~10, $\tilde{\sigma}_{\mathrm{L}}^{c,\lambda=1}$ changes very little. This shows that the ability of the NL part of σ to capture the long-range correlations makes an easier job for its L counterpart to capture the remaining physics.

To check the quality of the fit given in 40, we calculate the resulting $w_{\lambda=1}^{\mathrm{MRF}}(r_s)$. The relative error of $w_{\lambda=1}^{\mathrm{MRF}}(r_s)$ vs the exact $w_{\lambda=1}(r_s)$ [eq 36; PW92] as a function of r_s is shown in Figure 3.

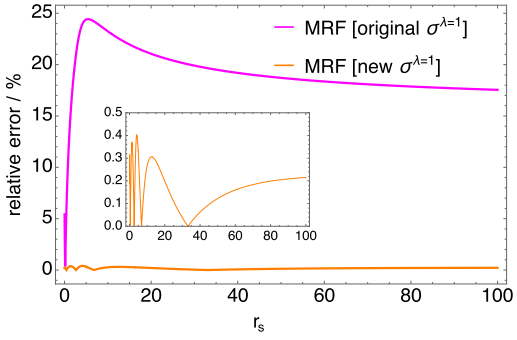

Figure 3. Relative error of $w_{\lambda=1}^{\mathrm{MRF}}(r_s)$ for the unpolarized UEG against the PW92 reference. "Original $\sigma^{\lambda=1}$" denotes the MRF results obtained with the original fluctuation function [eq 11]. "New $\sigma^{\lambda=1}$" denotes the MRF results obtained with the new fluctuation function [eq 37 with the NL part of eq 38 and the L part given by the fit of eq 40, and σ^{x} given by eq 35].

For comparison, we also show the relative error of $w_{\lambda=1}^{\mathrm{MRF}}(r_s)$ obtained with the original fluctuation function [eq 11]. Given the simplicity of the model and the fact that it has not been trained on the UEG, the relative error for the original MRF is reasonably small (never larger than 25%). On the other hand, the new fluctuation function [eq 37 with the NL part of eq 38 and the L part given by the fit of eq 40] yields $w_{\lambda=1}^{\mathrm{MRF}}(r_s)$, which is highly accurate for the UEG as the error in the underlying $w_{\lambda=1}^{\mathrm{MRF}}(r_s)$ never exceeds 0.5%. Furthermore, the relative error in $w_{\lambda=1}^{\mathrm{MRF}}(r_s)$ within the original $\sigma^{\lambda=1}$ does not vanish as $r_s \to 0$ (as it misses the $\tilde{\sigma}^{x}$ negative term of eq 35), whereas the new model also fixes that. We observe some oscillations in the error in this inset as r_s increases, and these would have likely diminished at small r_s if we had constrained the fit to match the exact next leading order for the UEG at the high-density limit.[50,51] At the same time, our fit for MRF yields the error that does not vanish in the low-density (large r_s limit) of UEG relative to the PW92 parameterization.[52] Yet, the magnitude of the error is energeti-

https://doi.org/10.1021/acs.jctc.3c00437
J. Chem. Theory Comput. 2023, 19, 6172−6184

cally negligible, as the overall error of 0.5% is within the PW92 reference's margin of error.[51]

5.3. More General Form for the Fluctuation Function Constrained by the UEG Condition. As an example of $\sigma_i^{\lambda}(\mathbf{r})$ at $\lambda = 1$ constrained by the UEG condition, we consider the following form

$$\sigma_i^{\lambda=1}(\mathbf{r}) = \tilde{\sigma}^{\mathrm{x}}(\mathbf{r}) + \underbrace{\frac{1}{2}\, e^{-bS_i(\mathbf{r})^2}}_{\sigma_{i,NL}^{c,\lambda=1}(\mathbf{r})} + \underbrace{\sigma_{\mathrm{UEG}}^{c,\lambda=1}(\mathbf{r})F(\mathbf{r})}_{\tilde{\sigma}_{\mathrm{L}}^{c,\lambda=1}(\mathbf{r})} \tag{41}$$

where $\sigma_{\mathrm{UEG}}^{c,\lambda=1}(\mathbf{r})$ at a given from $\rho(\mathbf{r})$ by using the fit from eq 40, and where $F(\mathbf{r})$ for now we simply set to

$$F(\mathbf{r}) = \frac{1}{1 + s(\mathbf{r})^2} \tag{42}$$

where $s(\mathbf{r})$ is the usual reduced density gradient $s(\mathbf{r}) = |\nabla\rho(\mathbf{r})|/(2(3\pi^2)^{1/3}\rho(\mathbf{r})^{4/3})$. This choice of $F(\mathbf{r})$ ensures that at $s = 0$, the high accuracy of the new fluctuation function for MRF is preserved for the UEG. In the rapidly varying limit ($s \to \infty$), correlation vanishes, and so does our $\tilde{\sigma}_{\mathrm{L}}^{c,\lambda=1}(\mathbf{r})$ term with this choice for $F(\mathbf{r})$. Nonnegativity of the sum of the correlation terms in eq 41 ensures that $w_{\lambda=1}^{\mathrm{MRF}}$ never lies above the exact $w_{\lambda=0}$, and this was not the case with the original MRF (eq 11).

5.4. Illustration: MRF XC Energy Densities for the Neon Atom at the Full Coupling Strength. Here we use the XC energy density to understand the terms of the fluctuation function of eq 41. The results with different options are shown in

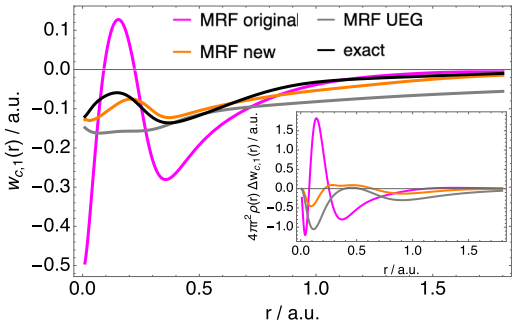

Figure 4. Correlation part of the XC energy densities at $\lambda = 1$ from the MRF functional with the fluctuation function of eq 41 with $F = 1$ ("MRF UEG") and F given by eq 42 ("MRF new"). The fluctuation function in "original MRF" is given by eq 11 [equal to only the second term of eq 41.] The MRF functional has been evaluated on the CCSD/aug-cc-pCVTZ densities, and the reference $w_{c,\lambda=1}(\mathbf{r})$ has been obtained by using the same level of theory and is taken from refs 29 and 30. Inset shows the errors in approximate $w_{c,\lambda=1}(\mathbf{r})$ multiplied by the density and spherical volume element.

Figure 4. In that figure, we show the correlation component of $w_{\lambda=1}(\mathbf{r})$, defined as

$$w_{c,\lambda}(\mathbf{r}) = w_{\lambda}(\mathbf{r}) - w_{\lambda=0}(\mathbf{r}) \tag{43}$$

If only the first term of eq 41 is used, the result reduces to the exact $w_{\lambda,0}(\mathbf{r})$ via rm-MRF (i.e., $w_{c,\lambda=1}^{\mathrm{MRF}}(\mathbf{r}) = 0$). If only the second term of eq 41 is used, the original $\sigma_i^{\lambda=1}(\mathbf{r})$ is recovered (eq 11), and the resulting $w_{\lambda=1}^{\mathrm{MRF}}(\mathbf{r})$ is labeled as "MRF original". This second term of eq 41 is essentially zero for the neon atom as all $S_i(\mathbf{r})$ values are large. Nonetheless, $\sigma = 0$ gives accurate $W_{\lambda=1}^{\mathrm{MRF}}$ for atoms, as mentioned earlier. Now we consider two different cases when all three terms of eq 41 are used. The first one with $F(\mathbf{r}) = 1$ ("MRF UEG"), and the other is with $F(\mathbf{r})$ given by eq 42 ("MRF new").

"MRF original" gets the shell structure of $w_{c,\lambda=1}^{\mathrm{MRF}}(\mathbf{r})$ right but overestimates its magnitude. As observed earlier, it becomes unphysically positive in the intershell region of atoms.[30] This cannot be the case with the fluctuations functions of eq 41, as its correlation part is always positive ensuring that: $w_{c,\lambda=1}^{\mathrm{MRF}}(\mathbf{r}) = w_{\lambda=1}^{\mathrm{MRF}}(\mathbf{r}) - w_{\lambda=0}(\mathbf{r}) \leq 0$. That is why the other two $w_{c,\lambda=1}^{\mathrm{MRF}}(\mathbf{r})$ in Figure 4 are negative everywhere since they are obtained from eq 41. While the magnitude of "MRF UEG" is reasonable, it misses the shell structure of the exact $w_{c,\lambda=1}(\mathbf{r})$. "MRF new" is the most accurate here and highlights the importance of using $F(\mathbf{r})$ in eq 41 to improve MRF. Also, the $s(\mathbf{r})$ quantity equips "MRF new" to capture the shell structure in the underlying correlation energy densities. This is further highlighted in Figure 5, where

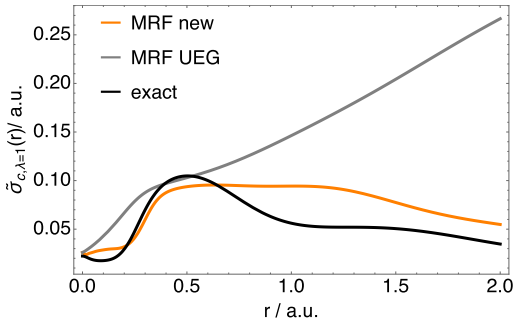

Figure 5. $\tilde{\sigma}_{\mathrm{L}}^{c,\lambda=1}(\mathbf{r})$ of eq 41 with $F = 1$ ("MRF UEG") and F given by eq 42 ("MRF new") for the neon atom. Since the NL term of eq 41 is essentially zero, we can compare shown $\tilde{\sigma}_{\mathrm{L}}^{c,\lambda=1}(\mathbf{r})$ with the "exact" $\tilde{\sigma}^{c,\lambda=1}(\mathbf{r})$ obtained via rm-MRF from eq 15. The computational details are the same as those from Figure 4.

we compare the underlying $\tilde{\sigma}_{\mathrm{L}}^{c,\lambda=1}(\mathbf{r})$ with "exact" $\tilde{\sigma}^{c,\lambda=1}(\mathbf{r})$ obtained via rm-MRF from accurate $w_{\lambda=1}(\mathbf{r})$ (further technical details are given in the caption of the figure). Note that such comparison is meaningful *only* if the i-dependent term of eq 41 (NL) is negligibly small, as is the case for the neon atom. From Figure 5, we can see that "MRF new" gives much more accurate $\tilde{\sigma}_{\mathrm{L}}^{c,\lambda=1}(\mathbf{r})$ than "MRF UEG". The former also builds a peak in $\tilde{\sigma}_{\mathrm{L}}^{c,\lambda=1}(\mathbf{r})$, which is necessary for the shell structure in the corresponding energy density. Also, at larger $\mathbf{r}$, where the density becomes small, "MRF UEG" over-correlates electrons (too large σ), while the $F(\mathbf{r})$ part containing $s(\mathbf{r})$ fixes this deficiency.

6. IMPLEMENTATION OF MRF

In this section, we outline the steps for the implementation of the MRF with Gaussian basis set for a given density. We first describe a refined scheme for the spherical average of two Gaussian functions that we need for the spherically averaged density $\tilde{\rho}(\mathbf{r}, u)$, an intermediate to the $N_e([\rho]; \mathbf{r}, u)$ integral, which is the key building block of MRF (eq 1). Then we explain our numerically robust scheme for computing the inverse of $N_e([\rho]; \mathbf{r}, u)$, which we also need for the MRF evaluation (eq 10). Finally, we introduce the algorithm for the reverse MRF machinery (Section 2.3), which, for example, enables us to "*translate*" the exact exchange energy density to MRF's fluctuation function—a starting point for building MRF's correlation on the top of exact exchange.

6.1. Spherically Averaged Electron Density with Hermite Gaussians. Here we greatly simplify the previous

https://doi.org/10.1021/acs.jctc.3c00437
J. Chem. Theory Comput. 2023, 19, 6172−6184

evaluations[28,53] of the spherically averaged (SA) density $\tilde{\rho}(\mathbf{r}, u)$ within the Gaussian basis set by using Hermite-Gaussians as intermediates. In the atomic orbital (AO) basis, the SA density (eq 2) becomes

$$\tilde{\rho}(\mathbf{r}, u) = \sum_{\mu\nu} D_{\mu\nu} \int \phi_\mu(\mathbf{r} + \mathbf{u}) \phi_\nu(\mathbf{r} + \mathbf{u}) \, \mathrm{d}\mathbf{\Omega}_\mathbf{u} \tag{44}$$

where $D_{\mu\nu}$ is the density matrix.

In practice, each basis function consists of several primitive Gaussians, with contraction coefficients $d_{\mu a}$

$$\phi_\mu(\mathbf{r}) = \sum_a d_{\mu a} \chi_a(\mathbf{r}) \tag{45}$$

For simplicity, we assume that all Gaussian basis functions contain only one primitive function, as the summation over primitives can be included in a straightforward way.

We separate the overlap between two primitive Cartesian Gaussians with exponents a and b and the origins $\mathbf{A}$ and $\mathbf{B}$ as

$$\begin{aligned} G_{ab}(\mathbf{r}) &= \chi_a(\mathbf{r}) \chi_b(\mathbf{r}) \\ &= G_{ij}^x(x, a, b, A_x, B_x) G_{kl}^y(y, a, b, A_y, B_y) G_{mn}^z \\ &\quad (z, a, b, A_z, B_z) \end{aligned} \tag{46}$$

Introducing a Hermite Gaussian positioned at the center of charge $\mathbf{P} = \frac{a\mathbf{A} + b\mathbf{B}}{p}$ and the total exponent $p = a + b$

$$\Lambda_t = \left(\frac{\partial}{\partial P_x} \right)^t \exp(-p x_P^2) \tag{47}$$

each Cartesian component for the overlap between two Gaussians may be expanded in terms of Hermite Gaussians and Hermite-to-Cartesian coefficients E_t^{ij} as follows

$$G_{ij} = \sum_{t=0}^{i+j} E_t^{ij} \Lambda_t \tag{48}$$

Note that the recursion relations are available for the E_t^{ij} coefficients.[54]

Then the total overlap over two Gaussians with a total azimuthal quantum number $(i + j + k + l + m + n)$ can be decomposed into a sum over Hermite Gaussians, which, in turn, can be expressed as derivatives of an s-type Hermite Gaussian (Λ_{000})

$$G_{ab}(\mathbf{r}) = \sum_{t=0}^{i+j} E_t^{ij} \sum_{u=0}^{k+l} E_u^{kl} \sum_{v=0}^{m+n} E_v^{mn} \Lambda_{tuv}(\mathbf{r}) \tag{49}$$

$$= \sum_{t=0}^{i+j} E_t^{ij} \sum_{u=0}^{k+l} E_u^{kl} \sum_{v=0}^{m+n} E_v^{mn} \left(\frac{\partial}{\partial P_x} \right)^t \left(\frac{\partial}{\partial P_y} \right)^u \left(\frac{\partial}{\partial P_z} \right)^v \Lambda_{000}(\mathbf{r}) \tag{50}$$

Defining the spherical average over the s-type Hermite Gaussian as follows

$$\Lambda_{000}^{\mathrm{SA}}(\mathbf{r}, u) = \frac{1}{4\pi} \int \Lambda_{000}(\mathbf{r} + \mathbf{u}) \, \mathrm{d}\mathbf{\Omega}_\mathbf{u} \tag{51}$$

and inserting the above expression for the overlap into eq 44 yields

$$\tilde{\rho}(\mathbf{r}, u) = \sum_{t=0}^{i+j} E_t^{ij} \sum_{u=0}^{k+l} E_u^{kl} \sum_{v=0}^{m+n} E_v^{mn} \left(\frac{\partial}{\partial P_x} \right)^t \left(\frac{\partial}{\partial P_y} \right)^u \left(\frac{\partial}{\partial P_z} \right)^v \Lambda_{000}^{\mathrm{SA}}(\mathbf{r}, u) \tag{52}$$

Equation 52 suggests that the spherical averaging can be performed before generating the pairs with higher azimuthal quantum numbers through differentiation with respect to the center of charge coordinates. Through the introduction of Hermite Gaussians and the associated recursion scheme for the Hermite-to-Cartesian coefficients, computation of the total coefficients by multiplying derivatives of the s-type Hermite Gaussians becomes much simpler in comparison to the previous scheme for the evaluation of the spherically averaged density.[28,53]

Finally, an expression for $\Lambda_{000}^{\mathrm{SA}}(\mathbf{r}, u)$ is obtained, considering that the spherical average over two s-type Cartesian Gaussian functions is given[53]

$$\frac{1}{4\pi} \int G_{ab}^{\mathrm{ss}}(\mathbf{r} + \mathbf{u}) = K_{ab} \exp(-p u^2) \frac{\sinh(\omega u)}{\omega u} \tag{53}$$

With the definitions of $\omega = 2|a\mathbf{r}_A + b\mathbf{r}_B|$ and the pre-exponential factor $K_{ab} = \exp\left(-\frac{ab}{a+b}(\mathbf{A} - \mathbf{B})^2\right)$, the spherical average of the 000-Hermite Gaussian is given by

$$\begin{aligned} \Lambda_{000}^{\mathrm{SA}}(\mathbf{r}, u) &= \frac{1}{4\pi} \int \exp(-p(\mathbf{r} + \mathbf{u} - \mathbf{P})^2) \, \mathrm{d}\Omega_u \\ &= \exp(-p u^2) \frac{\sinh(\omega u)}{\omega u} \end{aligned} \tag{54}$$

with ω now defined in terms of the center of charge coordinates ($\omega = 2pr_P$) and $r_P = |\mathbf{r} - \mathbf{P}|$. To go from $\tilde{\rho}(\mathbf{r}, u)$ to $N_e(\mathbf{r}, u)$, we need the integration of the s-type Hermite Gaussian over u, which can be performed analytically

$$4\pi \int_0^x u^2 \Lambda_{000}^{\mathrm{SA}}(\mathbf{r}, u) \, \mathrm{d}u = \mathrm{ifn}(\omega, p, x) \tag{55}$$

with the ifn function defined in ref 28.

In summary, eq 52 is the key equation for the simplified MRF calculation, which then together with eqs 54 and 55, can be used to compute the $N_e(\mathbf{r}, u)$ integral within a Gaussian basis set.

6.2. Implementation of an MRF with Variable Fluctuation Function. The key MRF building blocks described in the previous subsection and the MRF functional itself are implemented in a development version of the TURBOMOLE program.[38] The MRF XC energy densities (eq 8) are calculated on the usual real-space grids for semilocal XC functionals. At each grid point $\mathbf{r}$, we calculate the $N_e(\mathbf{r}, u)$ integral (the key MRF ingredient) and $\tilde{\rho}(\mathbf{r}, u)$ (needed for the MRF's fluctuation functions that employ $S_i(\mathbf{r})$ of eq 12). Both $N_e(\mathbf{r}, u)$ and $\tilde{\rho}(\mathbf{r}, u)$ are precomputed for a range of u interelectronic distances. Then the MRF energy density is computed following a stepwise procedure:

1. Sample the $N_e(\mathbf{r}, u)$ integral (eq 1) for a predefined range of the interelectronic distances u. Note that N_e monotonically increases with u and approaches N (number of electrons) at large u. We use 1000 grid points. The interval $[u_{\min}, u_{\max}]$ is adjusted at each $\mathbf{r}$ such that $N_e(\mathbf{r}, u_{\max}) \leq N - 0.0001$. In this way, we cover only the necessary u region and increase the overall accuracy of the approach.
2. Calculate the initial radii, $a_i(\mathbf{r})$, implicitly defined as: $N_e(\mathbf{r}, a_i(\mathbf{r})) = i - 1$ (eq 13). They are calculating by determining

https://doi.org/10.1021/acs.jctc.3c00437
J. Chem. Theory Comput. 2023, 19, 6172−6184

the bracketing values $u_m(\mathbf{r})$ and $u_{m+1}(\mathbf{r})$ for each $a_i(\mathbf{r})$, such that $u_m(\mathbf{r}) < a_i(\mathbf{r}) < u_{m+1}(\mathbf{r})$. Then $a_i(\mathbf{r})$ is calculated from a straight-line interpolation between $u_m(\mathbf{r})$ and $u_{m+1}(\mathbf{r})$ (see Figure 6 for an illustration). This interpolation scheme is robust and avoids numerical instabilities that may arise in nonlinear fits.

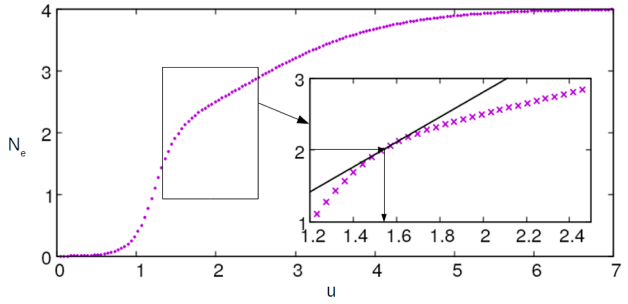

Figure 6. Large box: sampling of the $N_e(\mathbf{r}, u)$ integral for $r = 1.2$ bohr in the Be atom for various values of u. Magnified area: the initial radius of the third electron a_i is implicitly defined as $N_e(\mathbf{r}, a_3) = 2$ (eq 13) and found via straight line interpolation between the two points closest to $N_e = 2$.

3. Determine the fluctuation function of interest, $\sigma_i(\mathbf{r})$ for each i and $\mathbf{r}$, from the required building blocks. For example, the fluctuation function of eq 11 is calculated from $a_i(\mathbf{r})$ and the spherically averaged densities when $u = a_i(\mathbf{r})$.
4. Compute the multiple radii [$R_i(\mathbf{r})$ entering eq 8] via straight line interpolations, relying on the initial sampling of the $N_e(\mathbf{r}, u)$ again. In this way, the $N_e(\mathbf{r}, u)$ is calculated twice (at most), once for $a_i(\mathbf{r})$, and then for $R_i(\mathbf{r})$.
5. Calculate the MRF energy density (eq 8) from the radii and the precomputed Hartree potential.

This workflow is also presented in the pseudocode in Figure S2 in the Supporting Information.

6.3. Implementing the Reversed MRF Machinery. For the rm-MRF, described in Section 2.3, an average fluctuation function $\tilde{\sigma}$ has to be determined for a given input energy density $w_\lambda(\mathbf{r})$ at each grid point. To achieve this, we have adopted an approach similar to the calculation of the inverse electron number function described in Subsection 6.2: at each grid point, the energy density is calculated for a range of $\tilde{\sigma}$-values. The correct values for a given energy density are again obtained from a straight-line interpolation. In this fashion, we have obtained $\tilde{\sigma}^x(\mathbf{r})$ from $w_x(\mathbf{r}) = w_{\lambda=0}(\mathbf{r})$, but in principle, any input energy density (in the gauge of eq 7) can be used.

7. NUMERICAL EXAMPLES

In this section, we present data for different flavors of the MRF obtained in a post-SCF fashion, i.e., we use orbitals and densities obtained from a Hartree−Fock (HF) or KS-DFT calculation with a standard functional and evaluate only the XC energy with the MRF.

7.1. Energies for Atoms and Small Molecules. First, we consider a set of small (closed-shell) molecules shown in Figure 7 and the simplest possible case of the constant fluctuation function for MRF. We can see that a slightly negative fluctuation function, $\sigma_i^{\lambda=0}(\mathbf{r}) = -0.2$, already gives reasonable results for the $\lambda = 0$ case (total exchange energies) with an MAE of 0.11 hartree. This negative value of σ is in line with the previously observed range of exchange σ for, e.g., helium isoelectronic series[30] and in line with a slightly negative σ we find here for the UEG's exchange (eq 35). At the same time, this constant σ is the simplest case of the scale-invariable fluctuation function required for exchange (eq 20). Given the simple computational settings for the MRF calculations of Figure 7 (with a small basis set and a simple fluctuation function), these results can be used to rapidly validate new MRF codes (see also Table S1 for the raw data). In what follows, we will shift the focus of this section from the exchange to the $\lambda = 1$ case.

In Table 1, we show the computed XC integrand at the full coupling strength ($W_{\lambda=1}[\rho]$ of eq 4; physical electronic repulsion energy minus the Hartree energy). All MRF values have been obtained by using the MRF Gaussian basis solver described in Section 6 and the Hartree−Fock (HF) density. The second column shows the "MRF original" values, computed with the originally proposed fluctuation function [eq 11; the magenta curve in Figure 4]. The mean absolute error (MAE) of "MRF original" (here evaluated on the HF density) is only marginally different (0.01 hartree) from the previously computed[29] "MRF original" (evaluated on the CCSD density from the "grid-based" MRF solver). The second column shows "MRF new" [the fluctuation function given by eq 41 with F given by eq 42; the orange curve in Figure 4]. We design "MRF new" to ensure that its correlation energy densities are always negative, as this is not the case with "MRF original". Unfortunately, we can see from Table 1 that "MRF new" worsens "MRF original" for $W_{\lambda=1}[\rho]$ with the MAE twice as large.

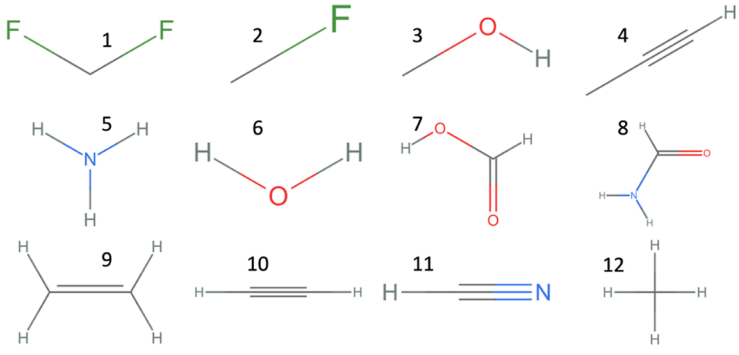

molecule	E_x	MRF; -0.2
1	-26.05	-26.07
2	-16.32	-16.42
3	-14.84	-14.93
4	-16.87	-16.70
5	-7.68	-7.91
6	-8.96	-9.28
7	-22.33	-22.35
8	-21.08	-21.05
9	-11.72	-11.76
10	-10.95	-11.00
11	-12.00	-12.11
12	-6.58	-6.73
	MAE	0.11

Figure 7. Exact exchange $E_x[\rho] = W_0[\rho]$ evaluated at the HF/def2-SVP level vs MRF's $W_\lambda[\rho]$ evaluated with the constant $\sigma = -0.2$ fluctuation function for a set of small molecules taken from ref 55. The exchange energies and densities have been obtained at the HF/def2-SVP level, and MRF has been obtained at the same densities. For raw data, see Table S1 in the Supporting Information, and for corresponding geometry files, see the Supporting Information as well. All energy values are shown in Hartree units.

https://doi.org/10.1021/acs.jctc.3c00437
J. Chem. Theory Comput. 2023, 19, 6172−6184

Table 1. $W_{\lambda_1}[\rho]$ (Eq 3; Electron Repulsion Energies at the Full Coupling Strength Minus the Hartree Energy) Obtained from "MRF Original" [Eq 11]; "MRF New" [the Fluctuation Function Given by Eq 41 with F Given by Eq 42]; and "MRF Optimized" [the Fluctuation Function Given by Eq 56 with 0.26, See Figure 8][a]

	MRF original	MRF new	MRF optimized	reference
He	−1.187	−1.082	−1.102	−1.103
Be	−2.807	−2.943	−2.849	−2.834
Ne	−12.859	−12.832	−12.771	−12.765
Mg	−16.362	−17.011	−16.689	−16.701
Ar	−31.193	−31.772	−30.990	−31.350
Ca	−35.896	−37.172	−36.180	−35.600
H^-	−0.542	−0.508	−0.498	−0.453
Li^-	−2.145	−2.243	−2.052	−1.946
F^-	−10.910	−11.002	−10.982	−10.889
Cl^-	−28.592	−29.314	−28.675	−28.890
MAE	0.160	0.339	0.153	

[a]All MRF energies have been calculated on the Hartree−Fock densities within the TZVP basis set[56] by using the MRF solver described in Section 6. The reference values (last column) have been calculated from CCSD and are taken from ref 29.

To preserve the accuracy of "MRF original" for atoms but still constrain the MRF correlation energy densities to always be negative, we consider the following proof-of-principle optimization of MRF with the following fluctuation function

$$\sigma_i^{\lambda=1}(\mathbf{r}) = \tilde{\sigma}^{\mathrm{x}}(\mathbf{r}) + \frac{d}{1+s\,\tilde{\sigma}_{\mathrm{L}}^{c,\lambda=1}(\mathbf{r})}\, e^{-d\rho(\mathbf{r})} \tag{56}$$

In Figure 8, we observe how the MAE in the resulting MRF's $W_{\lambda=1}[\rho]$ (for atoms/ions of Table 1) varies w.r.t. the d parameter. The lowest MAE is obtained at $d \sim \mathbf{0.26}$. With this choice of the fluctuation function, we restore the accuracy of "MRF original" for atoms while constraining its correlation energy densities to always be negative as in "MRF original". Equation 56 gives a starting point for the MRF optimization, and a more sophisticated version of this form will be explored in the future. Similarly, for a set of molecules considered in Figure 7, we find that the MAE of MRF with the σ of eq 56 for the electron repulsion energies ($\lambda = 1$ case) is also about 0.15 hartree vs the CCSD reference, with the d minimum slightly shifted toward smaller d values (see Figure S1 and Table S2 in the Supporting Information for further details).

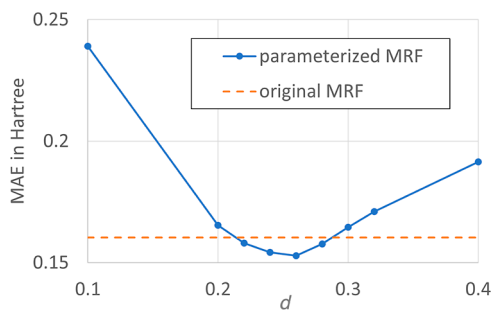

Figure 8. MAE in MRF's $W_{\lambda=1}[\rho]$ (eq 3; electron repulsion energies at the full coupling strength minus the Hartree energy) for the set of atoms(ions) of Table 1 with the d parameter in the underlying fluctuation function on eq 56. The optimal value of d is about 0.26.

7.2. rm-MRF Results. In Section 6.3, we described the implementation of rm-MRF, which we use here to translate $w_\lambda(\mathbf{r})$ at $\lambda = 0$ (exact exchange energy density) to $\tilde{\sigma}^{\mathrm{x}}(\mathbf{r})$. Figure 9 shows the $\tilde{\sigma}^{\mathrm{x}}(\mathbf{r})$ plots for the He, Be, and Ne atoms [panel (a)], along the internuclear axis of CO at equilibrium [panel (b)], along the molecular plane of benzene [panel (c)]. In all cases, $\tilde{\sigma}^{\mathrm{x}}(\mathbf{r})$ display distinct shell structure and varies between ∼−0.4 and ∼0.2 (for CO and benzene, it varies between ∼−0.2 and ∼0.2). These data are ideally suited for ML of the exchange part of MRF since a large amount of data can be generated from a small set of molecules since every grid point can be used as a datapoint in the training. In addition to these rm-MRF data for exchange, the simple UEG (eq 35) and scaling relation (eq 20) for MRF exchange can also be incorporated into the machine-learned MRF exchange models, and we will further explore this direction in future work.

7.3. MRF Model for the $\lambda \to \infty$ AC Limit. In the previous subsection, we have used the rm-MRF code to *translate* the exact exchange energy density into the "exact" $\tilde{\sigma}^{\lambda}(\mathbf{r})$. However, we note that rm-MRF can be used for translating any other energy density and at any λ (provided that is in the same gauge as MRF, that of eq 7) to MRF's i-averaged σ. We use now MRF to obtain the "exact" $\tilde{\sigma}^{\lambda}(\mathbf{r})$ from the (strongly interacting) $w_{\lambda\to\infty}(\mathbf{r})$ energy densities (see the left panel of Figure 10). In addition to the exact $w_{\lambda\to\infty}(\mathbf{r})$, we also use $w_{\lambda\to\infty}(\mathbf{r})$ from the shell model,[28] which gives the best approximation to $w_{\lambda\to\infty}(\mathbf{r})$ so far.[9] By "exact" $w_{\lambda\to\infty}(\mathbf{r})$, we refer to the one obtained from the specific "strictly correlated electrons" approach for spherically symmetric systems[23] (see ref 9 for further details). For comparison, we also show the weak coupling limit $\tilde{\sigma}^{\mathrm{x}}(\mathbf{r}) = \tilde{\sigma}^{\lambda=0}(\mathbf{r})$ quantity for Be, which, as previously observed, is mostly negative (except in the inter-shell region).[30] On the other hand, $\tilde{\sigma}^{\lambda\to\infty}(\mathbf{r})$ stays roughly around 1/2, with the maximum value of ∼0.8 at the nucleus [note from Section 4 that $\tilde{\sigma}^{\lambda=1}$ tends to ∼0.8 for the UEG in the low-density limit, the limit where $w_{\lambda=1}(\mathbf{r})$ tends to $w_{\lambda\to\infty}(\mathbf{r})$]. We can also see from the left panel of Figure 10 that the $\tilde{\sigma}^{\lambda\to\infty}(\mathbf{r})$ from the shell model is not a very good approximation to its "exact" counterpart [that is $\tilde{\sigma}^{\lambda\to\infty}(\mathbf{r})$ obtained from the reference $w_{\lambda\to\infty}(\mathbf{r})$ by rm-MRF]. Nevertheless, $w_{\lambda\to\infty}(\mathbf{r})$ from the shell model is highly accurate (see the right panel of Figure 10). This shows that one has some margin for error when modeling the MRF's fluctuation function, as the errors in the resulting XC energy densities are typically smaller than the errors in the fluctuation function. To further reinforce this point, and since $\tilde{\sigma}^{\lambda\to\infty}(\mathbf{r})$ is on average around 1/2, we investigate here the MRF model, where $\tilde{\sigma}^{\lambda\to\infty}(\mathbf{r})$ is simply always set to always to 1/2 ("MRF-half"). The resulting MRF-half $w_{\lambda\to\infty}(\mathbf{r})$ for the beryllium atom is shown in the right panel of Figure 10 and compared against its reference and shell model counterpart. We can see that the resulting MRF-half approximation displays point-wise accuracy very similar to the shell model, which is, as said, the most accurate approximation to $w_{\lambda\to\infty}(\mathbf{r})$ so far. Furthermore, MRF-half is even more accurate than the shell model at larger distances from the nucleus (see the inset in the right panel of Figure 10).

In addition to beryllium, in Figure 11, we also test the accuracy of $w_{\lambda\to\infty}(\mathbf{r})$ from MRF-half for the neon and argon atoms. For comparison, we also show accurate $w_{\lambda=0}(\mathbf{r})$ for the two atoms. From Figure 11, we can see that MRF-half also gives accurate $w_{\lambda\to\infty}(\mathbf{r})$ for Ne and Ar but displays fewer features than

https://doi.org/10.1021/acs.jctc.3c00437
J. Chem. Theory Comput. 2023, 19, 6172−6184

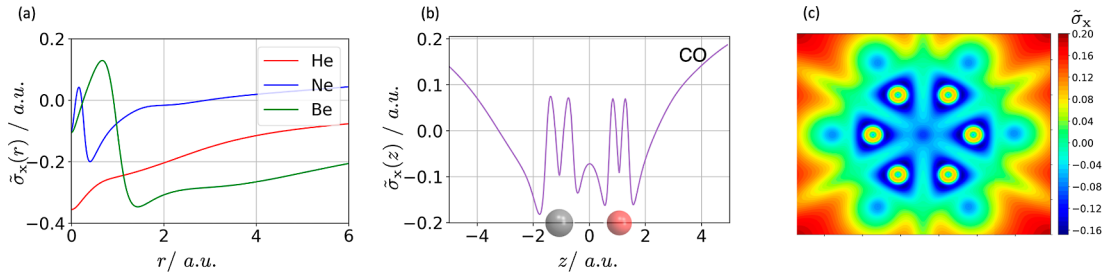

Figure 9. $\tilde{\sigma}^x(\mathbf{r})$ obtained from rm-MRF from the exact exchange energy density: (a) He, Be, and Ne atoms as a function of distance from the nucleus; (b) CO at equilibrium along the internuclear axis (positions of the two nuclei are shown); (c) benzene along the molecular plane. All exact exchange energy densities have been obtained at the HF/TZVP level.

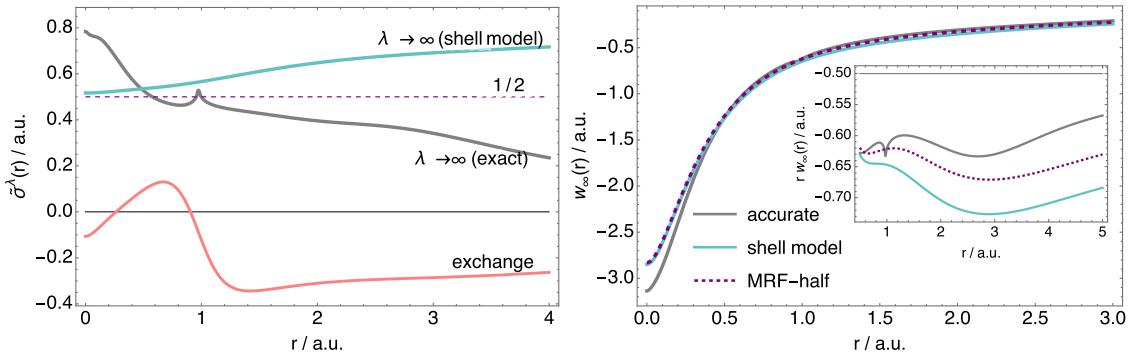

Figure 10. Left panel: $\tilde{\sigma}^\lambda(r)$ for the beryllium atom with distance from nucleus r. $\tilde{\sigma}^\lambda(r)$ is computed from the reverse MRF machinery (rm-MRF; Section 2.3). $\tilde{\sigma}^\lambda(r)$ is computed at $\lambda = 0$ from $w_{\lambda=0}(r)$ and from $w_{\lambda\to\infty}(r)$ (one coming from the shell model and the other coming from the exact $\lambda \to \infty$ limit). Right panel: $w_{\lambda\to\infty}(r)$ for the beryllium atom, comparison of the exact shell model and the one computed from MRF, where $\tilde{\sigma}(r)$ is set to 1/2 ("MRF-half"). The inset shows $w_{\lambda\to\infty}(r)$ multiplied by r.

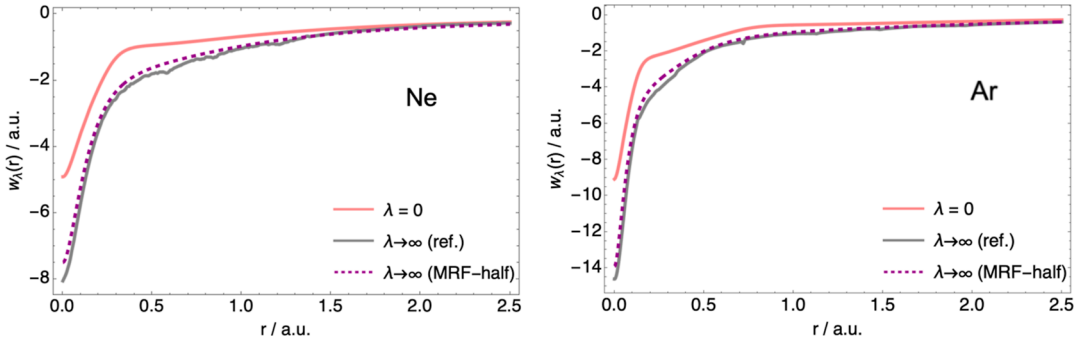

Figure 11. $w_{\lambda\to\infty}(r)$ exact and the one from MRF-half for the neon atom (left) and argon atom (right). $w_{\lambda=0}(r)$ (exchange) is also shown for comparison.

the exact $w_{\lambda\to\infty}(\mathbf{r})$. This would be likely fixed if one designs a more sophisticated $\tilde{\sigma}^{\lambda\to\infty}(\mathbf{r})$, by e.g., letting it vary between 1/2 and 0.8 (the maximum σ value from the UEG) and ensuring that it satisfies the scaling invariability constraint of eq 20 (this constraint is trivially satisfied in MRF-half, as $\tilde{\sigma}$ is always 1/2).

8. CONCLUSIONS

Here we make two key steps toward using MRF, a model inspired by the SIL of DFT, for the construction of robust exchange−correlation (XC) functionals that contain full spatial nonlocality. The first step is on the theory side, where we showed how the MRF model can be made exact for the UEG and how it should behave under the uniform density scaling. We then used these insights to construct improved fluctuation functions (a parametric object that determines the MRF functional). The second step is on the practical side, where we showed how the MRF functional can be implemented into standard (Gaussian basis set) quantum chemistry codes for a given density. This code and its results will be used to validate future MRF codes that will draw from further numerical approximations. For example, we expect that density fitting will greatly simplify the integral routines, speed up the MRF's evaluation, and facilitate the SCF implementations of the MRF functional.

With the affordable (N^3) nonlocality inspired by the SIL of DFT,—the use of MRF is very promising for the ML of the new generation of XC functionals. Specifically, we plan to construct MRF via ML of the fluctuation function of eq 41. In this equation, we have an exchange term that can be learned from the "exact MRF data" obtained from the "rm-MRF" procedure from the exact exchange energy density (Section 7.2). Then, in the correlation terms of the fluctuation function, we will distinguish the physics-based objects (e.g., the second term on the r.h.s.

https://doi.org/10.1021/acs.jctc.3c00437
J. Chem. Theory Comput. 2023, 19, 6172−6184

whose physics is described in ref 31 and the UEG part of the third term on the r.h.s. of eq 41) from the objects that will be machine learned. For example, F of eq 41 will be machine learned from the standard DFT (Jacob's ladder features) and MRF-specific fully nonlocal features [e.g., $S_i(\mathbf{r})$ and a_i of eqs 12 and 13, respectively].

Finally, the present paper also demonstrates the great versatility of the MRF functional for approximating different correlation regimes. While the original and very simple fluctuation function of eq 11 has been used to model $\lambda = 1$ quantities, here we also show that setting the fluctuation function simply to 1/2 delivers accurate local approximation for XC energy densities for the $\lambda \to \infty$ limit.

■ ASSOCIATED CONTENT

Supporting Information

The Supporting Information is available free of charge at https://pubs.acs.org/doi/10.1021/acs.jctc.3c00437.

Results and raw data pertaining to the set of molecules; MRF pseudocode figure (PDF)

XYZ coordinates of molecules of Figure 7 from ref 55. All molecules are singlet and 0 charge (TXT)

■ AUTHOR INFORMATION

Corresponding Authors

Stefan Vuckovic − *Department of Chemistry, University of Fribourg, 1700 Fribourg, Switzerland;* orcid.org/0000-0002-0768-9176; Email: stefan.vuckovic@unifr.ch

Hilke Bahmann − *Physical and Theoretical Chemistry, University of Wuppertal, 42119 Wuppertal, Germany*; Email: bahmann@uni-wuppertal.de

Complete contact information is available at: https://pubs.acs.org/10.1021/acs.jctc.3c00437

Notes

The authors declare no competing financial interest.

■ ACKNOWLEDGMENTS

S.V. acknowledges funding from the SNSF Starting Grant project (TMSGI2_211246). H.B. acknowledges funding from the Deutsche Forschungsgemeinschaft (DFG, German Research Foundation) project no. 4181400. We thank Paola Gori-Giorgi for insightful discussion which greatly improved the present work.

■ REFERENCES

(1) Mardirossian, N.; Head-Gordon, M. Thirty years of density functional theory in computational chemistry: an overview and extensive assessment of 200 density functionals. *Mol. Phys.* **2017**, *115*, 2315−2372.

(2) Goerigk, L.; Hansen, A.; Bauer, C.; Ehrlich, S.; Najibi, A.; Grimme, S. A look at the density functional theory zoo with the advanced GMTKN55 database for general main group thermochemistry, kinetics and noncovalent interactions. *Phys. Chem. Chem. Phys.* **2017**, *19*, 32184−32215.

(3) Verma, P.; Truhlar, D. G. Status and challenges of density functional theory. *Trends Chem.* **2020**, *2*, 302−318.

(4) Sim, E.; Song, S.; Vuckovic, S.; Burke, K. Improving Results by Improving Densities: Density-Corrected Density Functional Theory. *J. Am. Chem. Soc.* **2022**, *144*, 6625−6639.

(5) Burke, K. Perspective on density functional theory. *J. Chem. Phys.* **2012**, *136*, 150901.

(6) Cohen, A. J.; Mori-Sánchez, P.; Yang, W. Challenges for Density Functional Theory. *Chem. Rev.* **2012**, *112*, 289−320.

(7) Pribram-Jones, A.; Gross, D. A.; Burke, K. DFT: A Theory Full of Holes? *Annu. Rev. Phys. Chem.* **2015**, *66*, 283−304.

(8) Kalita, B.; Li, L.; McCarty, R. J.; Burke, K. Learning to Approximate Density Functionals. *Acc. Chem. Res.* **2021**, *54*, 818−826.

(9) Vuckovic, S.; Gerolin, A.; Daas, T. J.; Bahmann, H.; Friesecke, G.; Gori-Giorgi, P. Density functionals based on the mathematical structure of the strong-interaction limit of DFT. *Wiley Interdiscip. Rev.: Comput. Mol. Sci.* **2023**, *13*, No. e1634.

(10) Perdew, J. P.; Schmidt, K. Jacob's ladder of density functional approximations for the exchange-correlation energy. *AIP Conf. Proc.* **2001**, *577*, 1−20.

(11) Hammes-Schiffer, S. A conundrum for density functional theory. *Science* **2017**, *355*, 28−29.

(12) Pederson, R.; Kalita, B.; Burke, K. Machine learning and density functional theory. *Nat. Rev. Phys.* **2022**, *4*, 357−358.

(13) Kirkpatrick, J.; McMorrow, B.; Turban, D. H.; Gaunt, A. L.; Spencer, J. S.; Matthews, A. G.; Obika, A.; Thiry, L.; Fortunato, M.; Pfau, D.; et al. Pushing the frontiers of density functionals by solving the fractional electron problem. *Science* **2021**, *374*, 1385−1389.

(14) Vuckovic, S.; Irons, T. J. P.; Wagner, L. O.; Teale, A. M.; Gori-Giorgi, P. Interpolated energy densities, correlation indicators and lower bounds from approximations to the strong coupling limit of DFT. *Phys. Chem. Chem. Phys.* **2017**, *19*, 6169−6183.

(15) Vuckovic, S.; Wagner, L. O.; Mirtschink, A.; Gori-Giorgi, P. Hydrogen Molecule Dissociation Curve with Functionals Based on the Strictly Correlated Regime. *J. Chem. Theory Comput.* **2015**, *11*, 3153−3162.

(16) Chai, J.-D. Density functional theory with fractional orbital occupations. *J. Chem. Phys.* **2012**, *136*, 154104.

(17) Schmidt, J.; Benavides-Riveros, C. L.; Marques, M. A. L. Machine Learning the Physical Nonlocal Exchange−Correlation Functional of Density-Functional Theory. *J. Phys. Chem. Lett.* **2019**, *10*, 6425−6431.

(18) Nagai, R.; Akashi, R.; Sugino, O. Completing density functional theory by machine learning hidden messages from molecules. *npj Comput. Mater.* **2020**, *6*, 43.

(19) Margraf, J. T.; Reuter, K. Pure non-local machine-learned density functional theory for electron correlation. *Nat. Commun.* **2021**, *12*, 344.

(20) Li, L.; Hoyer, S.; Pederson, R.; Sun, R.; Cubuk, E. D.; Riley, P.; Burke, K. Kohn-Sham Equations as Regularizer: Building Prior Knowledge into Machine-Learned Physics. *Phys. Rev. Lett.* **2021**, *126*, 036401.

(21) Bystrom, K.; Kozinsky, B. CIDER: An Expressive, Nonlocal Feature Set for Machine Learning Density Functionals with Exact Constraints. *J. Chem. Theory Comput.* **2022**, *18*, 2180−2192.

(22) Seidl, M. Strong-interaction limit of density-functional theory. *Phys. Rev. A: At., Mol., Opt. Phys.* **1999**, *60*, 4387−4395.

(23) Seidl, M.; Gori-Giorgi, P.; Savin, A. Strictly correlated electrons in density-functional theory: A general formulation with applications to spherical densities. *Phys. Rev. A: At., Mol., Opt. Phys.* **2007**, *75*, 042511.

(24) Gori-Giorgi, P.; Vignale, G.; Seidl, M. Electronic Zero-Point Oscillations in the Strong-Interaction Limit of Density Functional Theory. *J. Chem. Theory Comput.* **2009**, *5*, 743−753.

(25) Buttazzo, G.; De Pascale, L.; Gori-Giorgi, P. Optimal-transport formulation of electronic density-functional theory. *Phys. Rev. A: At., Mol., Opt. Phys.* **2012**, *85*, 062502.

(26) Friesecke, G.; Gerolin, A.; Gori-Giorgi, P. The strong-interaction limit of density functional theory. **2022**, arXiv:2202.09760. arXiv preprint.

(27) Wagner, L. O.; Gori-Giorgi, P. Electron avoidance: A nonlocal radius for strong correlation. *Phys. Rev. A: At., Mol., Opt. Phys.* **2014**, *90*, 052512.

(28) Bahmann, H.; Zhou, Y.; Ernzerhof, M. The shell model for the exchange-correlation hole in the strong-correlation limit. *J. Chem. Phys.* **2016**, *145*, 124104.

(29) Vuckovic, S.; Gori-Giorgi, P. Simple Fully Nonlocal Density Functionals for Electronic Repulsion Energy. *J. Phys. Chem. Lett.* **2017**, *8*, 2799−2805.

(30) Vuckovic, S. Density functionals from the multiple-radii approach: analysis and recovery of the kinetic correlation energy. *J. Chem. Theory Comput.* **2019**, *15*, 3580−3590.
(31) Gould, T.; Vuckovic, S. Range-separation and the multiple radii functional approximation inspired by the strongly interacting limit of density functional theory. *J. Chem. Phys.* **2019**, *151*, 184101.
(32) Sun, J.; Ruzsinszky, A.; Perdew, J. P. Strongly constrained and appropriately normed semilocal density functional. *Phys. Rev. Lett.* **2015**, *115*, 036402.
(33) Perdew, J. P.; Burke, K.; Ernzerhof, M. Generalized Gradient Approximation Made Simple. *Phys. Rev. Lett.* **1996**, *77*, 3865−3868.
(34) Perdew, J. P.; Constantin, L. A.; Sagvolden, E.; Burke, K. Relevance of the Slowly Varying Electron Gas to Atoms, Molecules, and Solids. *Phys. Rev. Lett.* **2006**, *97*, 223002.
(35) Zhao, S.; Li, Z.-H.; Wang, W.-N.; Liu, Z.-P.; Fan, K.-N.; Xie, Y.; Schaefer, H. F. Is the uniform electron gas limit important for small Ag clusters? Assessment of different density functionals for Agn (n⩽4). *J. Chem. Phys.* **2006**, *124*, 184102.
(36) Cancio, A.; Chen, G. P.; Krull, B. T.; Burke, K. Fitting a round peg into a round hole: Asymptotically correcting the generalized gradient approximation for correlation. *J. Chem. Phys.* **2018**, *149*, 084116.
(37) Santra, B.; Perdew, J. P. Perdew-Zunger self-interaction correction: How wrong for uniform densities and large-Z atoms? *J. Chem. Phys.* **2019**, *150*, 174106.
(38) Balasubramani, S. G.; Chen, G. P.; Coriani, S.; Diedenhofen, M.; Frank, M. S.; Franzke, Y. J.; Furche, F.; Grotjahn, R.; Harding, M. E.; Hättig, C.; et al. TURBOMOLE: Modular program suite for ab initio quantum-chemical and condensed-matter simulations. *J. Chem. Phys.* **2020**, *152*, 184107.
(39) Langreth, D. C.; Perdew, J. P. The exchange-correlation energy of a metallic surface. *Solid State Commun.* **1975**, *17*, 1425−1429.
(40) Gunnarsson, O.; Lundqvist, B. I. Exchange and correlation in atoms, molecules, and solids by the spin-density-functional formalism. *Phys. Rev. B: Solid State* **1976**, *13*, 4274−4298.
(41) Vuckovic, S.; Irons, T. J. P.; Savin, A.; Teale, A. M.; Gori-Giorgi, P. Exchange−correlation functionals via local interpolation along the adiabatic connection. *J. Chem. Theory Comput.* **2016**, *12*, 2598−2610.
(42) Burke, K.; Cruz, F. G.; Lam, K.-C. Unambiguous exchange-correlation energy density. *J. Chem. Phys.* **1998**, *109*, 8161−8167.
(43) Vuckovic, S.; Levy, M.; Gori-Giorgi, P. Augmented potential, energy densities, and virial relations in the weak-and strong-interaction limits of DFT. *J. Chem. Phys.* **2017**, *147*, 214107.
(44) Armiento, R.; Mattsson, A. E. Subsystem functionals in density-functional theory: Investigating the exchange energy per particle. *Phys. Rev. B: Condens. Matter Mater. Phys.* **2002**, *66*, 165117.
(45) Vuckovic, S.; Irons, T.; Savin, A.; Teale, A. M.; Gori-Giorgi, P. Exchange−correlation functionals via local interpolation along the adiabatic connection. *J. Chem. Theory Comput.* **2016**, *12*, 2598−2610.
(46) Levy, M.; Perdew, J. P. Hellmann−Feynman, virial, and scaling requisites for the exact universal density functionals. Shape of the correlation potential and diamagnetic susceptibility for atoms. *Phys. Rev. A: At., Mol., Opt. Phys.* **1985**, *32*, 2010−2021.
(47) Levy, M.; Perdew, J. P. Tight bound and convexity constraint on the exchange-correlation-energy functional in the low-density limit, and other formal tests of generalized-gradient approximations. *Phys. Rev. B: Condens. Matter Mater. Phys.* **1993**, *48*, 11638−11645.
(48) https://mathworld.wolfram.com/HurwitzZetaFunction.html (Online; accessed July 12, 2023).
(49) Wolfram Research, Inc. *Mathematica*, Version 13.3. https://www.wolfram.com/mathematica (online; accessed July 12, 2023).
(50) Perdew, J. P.; Wang, Y. Accurate and simple analytic representation of the electron-gas correlation energy. *Phys. Rev. B: Condens. Matter Mater. Phys.* **1992**, *45*, 13244−13249.
(51) Bhattarai, P.; Patra, A.; Shahi, C.; Perdew, J. P. How accurate are the parametrized correlation energies of the uniform electron gas? *Phys. Rev. B* **2018**, *97*, 195128.
(52) Seidl, M.; Vuckovic, S.; Gori-Giorgi, P. Challenging the Lieb−Oxford bound in a systematic way. *Mol. Phys.* **2016**, *114*, 1076−1085.
(53) Antaya, H.; Zhou, Y.; Ernzerhof, M. Approximating the exchange energy through the nonempirical exchange-factor approach. *Phys. Rev. A: At., Mol., Opt. Phys.* **2014**, *90*, 032513.
(54) Helgaker, T.; Jørgensen, P.; Olsen, J. *Molecular Electronic-Structure Theory*; John Wiley Sons, Ltd., 2000; Chapter 9, pp 336−432.
(55) Goerigk, L.; Hansen, A.; Bauer, C.; Ehrlich, S.; Najibi, A.; Grimme, S. A look at the density functional theory zoo with the advanced GMTKN55 database for general main group thermochemistry, kinetics and noncovalent interactions. *Phys. Chem. Chem. Phys.* **2017**, *19*, 32184−32215.
(56) Schäfer, A.; Huber, C.; Ahlrichs, R. Fully optimized contracted Gaussian basis sets of triple zeta valence quality for atoms Li to Kr. *J. Chem. Phys.* **1994**, *100*, 5829−5835.

https://doi.org/10.1021/acs.jctc.3c00437
J. Chem. Theory Comput. 2023, 19, 6172−6184